Supplementary information

Mapping the emergence of molecular vibrations mediating bond formation

In the format provided by the authors and unedited

Jong Goo Kim, Shunsuke Nozawa, Hanui Kim, Eun Hyuk Choi, Tokushi Sato, Tae Wu Kim, Kyung Hwan Kim, Hosung Ki, Jungmin Kim, Minseo Choi, Yunbeom Lee, Jun Heo, Key Young Oang, Kouhei Ichiyanagi, Ryo Fukaya, Jae Hyuk Lee, Jaeku Park, Intae Eom, Sae Hwan Chun, Sunam Kim, Minseok Kim, Tetsuo Katayama, Tadashi Togashi, Sigeki Owada, Makina Yabashi, Sang Jin Lee, Seonggon Lee, Chi Woo Ahn, Doo-Sik Ahn, Jiwon Moon, Seungjoo Choi, Joonghan Kim, Taiha Joo, Jeongho Kim, Shin-ichi Adachi & Hyotcherl Ihee[✉]

Supplementary Information

Supplementary Text

1. Generation of time-resolved difference scattering curves

Two-dimensional scattering images recorded on the CCD detector were azimuthally averaged to give one-dimensional scattering curves, $S(q,t)$, as a function of momentum transfer, q, and time delay, t, between the laser and x-ray pulses. Time-resolved difference scattering curves, $\Delta S(q,t)$, were generated by subtracting the reference data measured at -20 ps from the data at other time delays. The two-dimensional scattering images can in principle have anisotropic component arising from the anisotropic orientational distribution of excited molecules. The difference scattering intensity of a two-dimensional difference scattering image can be decomposed as

$$\Delta S(\vec{q},\theta_{\vec{q}},t) \propto \Delta S_0(\vec{q},t) - P_2(\cos\theta_{\vec{q}})\Delta S_2(\vec{q},t) \tag{S1}$$

where, $\vec{q}$ is the scattering vector, $\theta_{\vec{q}}$ is the angle between the laser polarization axis and $\vec{q}$, $\Delta S_0(\vec{q},t)$ and $\Delta S_2(\vec{q},t)$ are the isotropic and anisotropic difference scattering intensities, and P_2 is the second-order Legendre polynomial. From the linear relation between $\Delta S(\vec{q},\theta_{\vec{q}},t)$ and $P_2(\cos\theta_{\vec{q}})$, $\Delta S_0(\vec{q},t)$ and $\Delta S_2(\vec{q},t)$ can be extracted. $\Delta S(\vec{q},\theta_{\vec{q}},t)$ were plotted with respect to $P_2(\cos\theta_{\vec{q}})$ for a specific $\vec{q}$ value, then the data points were fit by a straight line. According to Eq. (S1), the intercept with the $P_2 = 0$ axis and the slope of the fit line are the isotropic scattering intensity, ΔS_0, and the anisotropic scattering intensity, ΔS_2, respectively. It can be seen that the azimuthally-averaged difference scattering curves and the isotropic scattering curves, ΔS_0, are identical to each other within experimental errors (Fig. S1). Thus, in this work, we used the azimuthally-averaged difference scattering curves, rather than isotropic difference scattering curves, without the need of correcting the anisotropic contribution.

2. Determination of equilibrium structures of S_0, T_1', and T_1 states

As described in Methods, we eliminated the exponential components from $\Delta S(q,t)$ to extract $\Delta S_{residual}(q,t)$. Those exponential components, termed as $\Delta S'(q,t)$, consist of $\Delta S_{transit}(q,t)$ and $\Delta S_{heat}(q,t)$ as can be seen in Eq. (2) in Methods. We refined the equilibrium structures of S_0, T_1', and T_1 states based on $\Delta S'(q,t)$. To refine the equilibrium structures, theoretical difference scattering intensities, $\Delta S_{theory}'(q,t)$, were constructed using Eqs. (2) – (4) in Methods as follows:

$$\Delta S_{theory}'(q,t) = c_{T_1'}(t)(S_{T_1'^{eq}}(q) - S_{S_0^{eq}}(q)) + c_{T_1}(t)(S_{T_1^{eq}}(q) - S_{S_0^{eq}}(q)) + \Delta S_{heat}(q)\Delta T(t) \qquad (S2)$$

where $\Delta T(t)$ is temperature change at each time delay, and $\Delta S_{heat}(q)$ represents scattering intensity change with respect to the increase of solvent temperature.

As fitting parameters of the analysis, we considered two adjacent Au–Au distances (R_{AB} and R_{BC}), and a bond angle (Au–Au–Au angle) for the S_0, T_1', and T_1 states, a scaling factor between the experimental and theoretical scattering intensities, and temperature change, $\Delta T(t)$. $\Delta S_{heat}(q)$ was determined from a separate TRXL experiment on 40 mM $FeCl_3$ solution to measure the difference scattering signal arising purely from solvent heating, as shown in Extended Data Fig. 8a. The experimental difference scattering curves of $FeCl_3$ solution were obtained at time delays from –740 fs to 2260 fs with a time step of 25 fs. As can be seen in the results of the SVD analysis on the TRXL data of $FeCl_3$ solution shown in Extended Data Figs. 8b and 8c, only one significant singular component was identified, indicating that a single difference scattering curve (that is, the first lSV) can account for the contribution of solvent heating at the measured time delays. Thus, the first lSV was used as $\Delta S_{heat}(q)$.

Scattering intensity arising from a molecular structure was calculated using the following Debye equation,

$$S(q) = 3F_{Au}^2(q) + 2F_{Au}^2(q)\left(\frac{\sin(qR_{AB})}{qR_{AB}} + \frac{\sin(qR_{BC})}{qR_{BC}} + \frac{\sin(qR_{AC})}{qR_{AC}} \right) \qquad (S3)$$

where $F_{Au}(q)$ is the atomic form factor of the Au atom. The maximum likelihood estimation (MLE) with the χ^2 estimator was employed to minimize the discrepancy between $\Delta S'(q,t)$ and $\Delta S_{theory}'(q,t)$. The chi-square (χ^2) is given by the following equation:

$$\chi^2 = \frac{1}{n_q n_t - p - 1} \sum_{i}^{n_q} \sum_{j}^{n_t} \frac{(c_s \Delta S_{theory}'(q_i,t_j) - \Delta S'(q_i,t_j))^2}{\sigma_{ij}^2} \tag{S4}$$

where n_q is the number of fitted q points, n_t is the number of fitted time delays, p is the number of fitting parameters, σ_{ij} is the standard deviation, and c_s is the scaling factor between theoretical and experimental difference curves. The minimization was performed by the MINUIT software package and the error values were provided by MINOS algorithm in MINUIT.

For S_0 and T_1', Debye-Waller factors (DWFs) were introduced to consider distributions of interatomic distances arising from the weak Au–Au bonding in S_0 and the spatial broadening of the initially created wave packet, which is induced by finite pulse duration of the pump pulse, on the PES of T_1', respectively. In contrast, DWFs for T_1 were not used for the fitting since it did not improve the fitting quality any further. We note that DWFs were used in the structural analysis to describe the ensemble of heterogeneous Au-Au distances although DWFs are commonly used to describe the time-averaged distribution of interatomic distances due to thermal fluctuation. When including the DWFs, Eq. (S3) is modified as follows.

$$S(q) = 3F_{Au}^2(q) + 2F_{Au}^2(q)\left(\frac{\sin(qR_{AB})}{qR_{AB}} e^{-\frac{\sigma_1^2 q^2}{2}} + \frac{\sin(qR_{BC})}{qR_{BC}} e^{-\frac{\sigma_1^2 q^2}{2}} + \frac{\sin(qR_{AC})}{qR_{AC}} e^{-\frac{\sigma_2^2 q^2}{2}} \right) \tag{S5}$$

where σ_1^2 is the mean-squared displacement for R_{AB} and R_{BC} and σ_2^2 is the mean-squared displacement for R_{AC}.

Following the results of the previous TRXL study on $[Au(CN)_2^-]_3$[9], it was assumed that T_1' and T_1 have linear and symmetric structures (that is, $R_{AB} = R_{BC} = 2.82$ Å for T_1' and $R_{AB} = R_{BC} = 2.71$ Å for T_1). In contrast, in the previous TRXL study, the equilibrium structure of S_0 was not clearly determined, whether it is symmetric or asymmetric. Since a better signal-to-noise ratio was achieved in the TRXL data presented in this work, we were able to determine the structure of S_0. In the previous TRXL study[9], both asymmetric and

symmetric equilibrium structures of S_0 gave equivalently good fits to the experimental data when appropriate DWFs were used. In this work, the exponential components, $\Delta S'(q,t)$, are also fit equally well with both symmetric and asymmetric structures of S_0. The refined structural parameters obtained from the fitting of $\Delta S'(q,t)$ are listed in Table S1. However, as discussed in Methods, structural analysis using residual difference scattering curves reveals that the asymmetric equilibrium structure of S_0 gives much better fits to the residual difference scattering curves, confirming that the equilibrium structure of S_0 is asymmetric.

3. Assignment of activated vibrational modes of the wave packet

To identify the origin of the oscillations observed in $q\Delta S_{residual}(q,t)$, we inspected the structural changes of $[Au(CN)_2^-]_3$ in S_0 and T_1'. In Section "Structural analysis using residual difference scattering curves" of Methods, we showed that the excited-state wave packet in T_1' exhibits only symmetric stretching vibrations, allowing us to approximate the transient structure of T_1' as symmetric and linear ($R_{AB} = R_{BC}$, $\theta = 180\,°$) at all time delays. To assign the symmetric stretching vibrations to specific vibrational normal modes of T_1', we fitted time-dependent Au–Au distances, $R_{AB}(t)$, $R_{BC}(t)$, and $R_{AC}(t)$, of T_1', which was determined by the structural analysis, using a sum of damping cosine functions. Specifically, time-dependent Au–Au distances were described by a sum of damping cosine functions, $R_{AB}{}^{thy}(t)$, $R_{BC}{}^{thy}(t)$, and $R_{AC}{}^{thy}(t)$ as follows:

$$R_{AB}{}^{thy}(t) = R_{AB}{}^{T_1'eq} + \sum_i^n A_i \cos(2\pi ct\nu_i + \phi_i)\exp(-t/\tau_i)$$
$$R_{BC}{}^{thy}(t) = R_{AB}{}^{thy}(t) \tag{S6}$$
$$R_{AC}{}^{thy}(t) = 2R_{AB}{}^{thy}(t)$$

where $R_{AB}{}^{T_1'eq}$ is the R_{AB} in the equilibrium structure of T_1', A_i, ν_i, ϕ_i, and τ_i are the amplitude, frequency, phase, and damping constant of a damping cosine function, respectively, and n is the number of damping cosine functions used for the fitting. The discrepancy, Δ, between the experimentally-resolved Au–Au distances of T_1', $R_{AB}(t)$, $R_{BC}(t)$, and $R_{AC}(t)$, and the theoretical Au–Au distances described by the damping cosine functions, $R_{AB}{}^{thy}(t)$, $R_{BC}{}^{thy}(t)$, and $R_{AC}{}^{thy}(t)$, is defined by the following equation:

4

$$\Delta = \sum_{i}^{n_t} \{R_{AB}{}^{thy}(t_i) - R_{AB}(t_i)\}^2 + \{R_{BC}{}^{thy}(t_i) - R_{BC}(t_i)\}^2 + \{R_{AC}{}^{thy}(t_i) - R_{AC}(t_i)\}^2 \qquad (S7)$$

where n_t is the number of fitted time delays. For the fitting, Δ was minimized by adjusting fitting parameters (A_i, ϕ_i, and τ_i). In this fitting, the frequencies, ν_i, of the damping cosine functions were chosen from the frequencies of three peaks identified in the Fourier spectrum in Fig. 4c (32 cm^{-1}, 79 cm^{-1}, and 125 cm^{-1}). Initially, the fitting was tried with a single damping cosine function (that is, $n = 1$ in Eq. (S6)) by selecting one oscillating frequency from the three Fourier frequencies, 32 cm^{-1}, 79 cm^{-1} and 125 cm^{-1}. In this case, the experimentally resolved interatomic Au–Au distances of T$_1$' are not fit satisfactorily. Then, we tried the fitting using two damping cosine functions (that is, $n = 2$ in Eq. (S6)) by selecting two oscillating frequencies from the three Fourier frequencies, 32 cm^{-1}, 79 cm^{-1}, and 125 cm^{-1}. The damping cosine functions of 79 cm^{-1} and 125 cm^{-1} frequencies give satisfactory fits to the R$_{AB}$(t), R$_{BC}$(t), and R$_{AC}$(t), of T$_1$', as shown in Fig. 2c. Therefore, the symmetric stretching vibrations of T$_1$' correspond to two symmetric stretching modes with the 79 cm^{-1} and 125 cm^{-1} frequencies.

To relate those experimentally identified vibrational modes with theoretical normal modes, we examined the normal modes of a triplet state obtained from DFT calculation, as shown in Extended Data Fig. 6. Among the theoretical normal modes of the triplet state, there are two symmetric stretching modes, T$_1$_#6 (63 cm^{-1}) and T$_1$_#12 (92 cm^{-1}). Therefore, we assigned the two oscillations of 79 cm^{-1} and 125 cm^{-1} frequencies observed in TRXL data to T$_1$_#6 and T$_1$_#12 modes of the excited state, T$_1$', respectively.

Similarly, for S$_0$, we tried to fit time-dependent Au–Au distances, R$_{AB}$(t), R$_{BC}$(t), and R$_{AC}$(t), of S$_0$ by a sum of damping cosine functions. Among the three Fourier frequencies, the 79 cm^{-1} and 125 cm^{-1} frequencies were assigned to the excited-state wave packets in T$_1$', leaving only the 32 cm^{-1} frequency unassigned. However, the time dependent Au–Au distances of S$_0$ shown in Fig. 2e were not fit satisfactorily using a single damping cosine function with 32 cm^{-1} frequency. Thus, we performed another type of fitting analysis to identify the ground-state wave packets created in S$_0$ as follows. In principle, the time-dependent Au–Au distances of S$_0$ can be described by a combination of normal modes obtained from DFT calculation for S$_0$, of which the displacement vectors are shown in

Extended Data Fig. 5. In detail, the time-dependent Au–Au distances, $R_{AB}(t)$, $R_{BC}(t)$, and $R_{AC}(t)$, of S_0 were fit by theoretical Au–Au distances that were constructed with a combination of displacement vectors of candidate normal modes.

To calculate the theoretical Au–Au distances described by the normal mode vibrations, $R_{AB}^{NM}(t)$, $R_{BC}^{NM}(t)$, and $R_{AC}^{NM}(t)$, we assumed that the structure of S_0 vibrates following the displacement vectors of candidate normal modes and each normal mode was modeled to damp exponentially. Accordingly, time-dependent molecular structure of S_0 at a time delay, t, was described as follows,

$$R_{S_0}^{NM}(t) = R_{S_0^{eq}} + \sum_i^N D_{NM_i} A_{NM_i} \cos(2\pi ct\nu_{NM_i} + \phi_{NM_i}) \exp(-t/\tau_{NM_i}) \tag{S8}$$

where $R_{S_0}^{NM}(t)$ and $R_{S_0^{eq}}$ are 3×3 matrices whose row vectors are three-dimensional coordinates that indicate the positions of the three Au atoms at t and in the equilibrium structure of S_0, respectively, D_{NM_i} is a 3×3 matrix whose row vectors are three-dimensional displacement vectors of the three Au atoms for each normal mode, A_{NM_i} is the scaling factor for the vibrational amplitude of each mode, ν_{NM_i} is the oscillating frequency of each mode, ϕ_{NM_i} is the phase of each mode, τ_{NM_i} is the damping time constant of each mode, c is the speed of light, and N is the number of normal modes used for the fitting. Using the three-dimensional coordinates of Au atoms in a transient molecular structure of S_0, $R_{S_0}^{NM}(t)$, described by Eq. (S8), Au–Au distances changed by normal mode vibrations, $R_{AB}^{NM}(t)$, $R_{BC}^{NM}(t)$, and $R_{AC}^{NM}(t)$, were calculated.

The discrepancy, Δ', between the experimentally-resolved Au–Au distances of S_0, $R_{AB}(t)$, $R_{BC}(t)$, and $R_{AC}(t)$, shown in Fig. 2e and the theoretical Au–Au distances described by the normal mode vibrations, $R_{AB}^{NM}(t)$, $R_{BC}^{NM}(t)$, and $R_{AC}^{NM}(t)$, is defined by the following equation:

$$\Delta' = \sum_i^{n_t} \{R_{AB}^{NM}(t_i) - R_{AB}(t_i)\}^2 + \{R_{BC}^{NM}(t_i) - R_{BC}(t_i)\}^2 + \{R_{AC}^{NM}(t_i) - R_{AC}(t_i)\}^2 \tag{S9}$$

where n_t is the number of fitted time delays. For the fitting, Δ' was minimized by adjusting fitting parameters (A_{NM_i}, ν_{NM_i}, ϕ_{NM_i}, and τ_{NM_i}). We note that, in this fitting analysis for the ground-state wave packet motion, a theoretical vibrational motion of each normal mode determined by displacement vectors was used intactly, whereas a vibrational frequency of each normal mode was adjusted as a fitting parameter.

First, we tried this fitting analysis for the ground-state wave packet motion using a single mode among the normal modes of S_0 shown in Extended Data Fig. 5 ($N = 1$ in Eq. (S8)), and we found that the experimentally resolved interatomic Au–Au distances, $R_{AB}(t)$, $R_{BC}(t)$, and $R_{AC}(t)$, of S_0 cannot be fit decently by any single normal mode. Then, we performed the fitting using two normal modes of S_0 ($N = 2$ in Eq. (S8)). Among all the possible combinations, the best fits to $R_{AB}(t)$, $R_{BC}(t)$, and $R_{AC}(t)$ of S_0 were obtained when using a symmetric stretching mode ($S_0\_\#6$) and an asymmetric stretching mode ($S_0\_\#5$), of which the oscillation frequencies were determined to be 32 cm^{-1} and 44 cm^{-1}, respectively, from the fitting (Fig. 2e). Thus, we concluded that a symmetric stretching mode with 32 cm^{-1} frequency and an asymmetric stretching mode with 44 cm^{-1} frequency are the active ground-state wave packets in S_0.

4. Assignment of electronic states

In transient absorption (TA)[17] and time-resolved luminescence studies[18] on $[Au(CN)_2^-]_3$, an additional kinetic component with a time constant of 500 fs and ~20 fs, respectively, were observed and assigned to the intersystem crossing (ISC) from the initially excited singlet state (S_1) to a triplet excited state, but that component was not observed by TRXL[9], suggesting that the intersystem crossing does not involve any significant structural change. Considering the similar structures of the excited singlet and triplet states and the sensitivity of spectroscopic signal to the population of electronic states, the initially excited state identified by TRXL can be practically considered as the triplet state reached by ISC transition, as discussed in our previous publication[9]. We note that, in this work, the triplet excited state reached by ISC and another triplet excited state formed by subsequent bond contraction are termed T_1' and T_1, respectively, following the notations in our previous publication[9]. On the contrary, those states were labeled as T_1 and T_1', respectively, in the time-resolved luminescence study[18].

5. Assignment of activated vibrational normal modes based on their frequencies

The frequencies of the oscillations observed in $q\Delta S_{residual}(q,t)$ were extracted from the Fourier power spectrum of $q\Delta S_{residual}(q,t)$ in the late time range (> 360 fs). As shown in Fig. 4c, the FT spectrum shows a major peak with the largest intensity at 32 cm^{-1} frequency, and minor peaks at 79 cm^{-1} and 125 cm^{-1} frequencies. First, we note that the four oscillation frequencies (79 cm^{-1} and 125 cm^{-1} for T_1', 32 cm^{-1} and 44 cm^{-1} for S_0) were identified by inspecting time-dependent structural changes of the gold trimer complex, whereas only three oscillation frequencies were identified in the FT spectrum, indicating that the peak at 44 cm^{-1} frequency is masked by the broad peaks at other frequencies. This observation indicates that the assignment of the molecular vibrations only based on the frequency information may mispredict the number of activated vibrational modes. Moreover, the oscillations can be assigned to irrelevant vibrational modes. For example, if one attempts to assign the vibration of 32 cm^{-1} frequency solely based on the frequency information, he will examine normal modes of S_0 and T_1 calculated by DFT calculations in a wide range of frequencies around 32 cm^{-1} (for example from 20 cm^{-1} to 60 cm^{-1}), considering the global sensitivity of TRXL signal to various electronic states and the limited accuracy of DFT calculation of vibrational frequencies. Among the normal modes of the two electronic states, there are a total of eleven normal modes (six and five normal modes for S_0 and T_1, respectively) with frequencies in the range of 20 – 60 cm^{-1} as shown in Fig. 4c. More details of these normal modes can be seen in Extended Data Figs. 5 and 6. Among the eleven modes, if one follows the normal practice to choose the normal mode with the most similar frequency as the 32 cm^{-1} frequency, a bending mode of T_1 with frequency of 33 cm^{-1} would be chosen. However, as revealed from the structural changes of T_1', the 32 cm^{-1} oscillation corresponds to the symmetric stretching mode of S_0, not the bending mode of T_1'.

6. Initial motion of the ground-state wave packet in S_0

The ground-state wave packet moves in the direction of decreasing R_{AB} and increasing θ within 100 fs, prior to returning toward the equilibrium structure of S_0. Such initial motion of the ground-state wave packet occurs because it is affected by the initial motion of the excited-state wave packet. Since the optical pump pulse has a finite duration, the second interaction with the pump pulse for impulsive Raman scattering can occur with a

certain time delay (that is, non-impulsively) after the first interaction within the pulse duration (~100 fs). As a result, the second interaction with the pump pulse would occur after the evolution of wave packet in the excited state for the pulse duration and thus create the ground-state wave packet at a position off the equilibrium structure of the ground state, toward the direction of the excited-state wave packet motion. After 100 fs time delay, the effect of finite pulse duration would be saturated and the ground-state wave packet returns toward the equilibrium structure of S_0.

7. Contributions from carbon and nitrogen atoms and the cage term

In the structural analysis presented in this work, we considered only three Au atoms to calculate the scattering intensity of the gold trimer complex because the contribution of CN^- ligands to the scattering intensity is negligible. A gold atom has much more electrons (79 electrons) than a carbon (6 electrons) or a nitrogen (7 electrons) atom and the number ratio of the gold atoms with respect to carbon and nitrogen atoms is rather large (1:2 for both carbon and nitrogen), so that the scattering intensity from gold atoms is expected to be much stronger than the scattering intensity from carbon or nitrogen atoms. We calculated the difference scattering curve from all the atoms in the gold trimer complex and compared it with the difference scattering curve from the three Au atoms and the results are shown in Fig. S2a. As expected based on the number of electrons in each atom and the number ratio, the scattering intensity from CN^- ligands is negligibly small compared with the scattering intensity from Au atoms. For comparison, we examined the effect of ligands on the scattering intensity in the cases of $[Ir_2(dimen)_4]^{2+}$ and $[Pt_2(P_2O_5H_2)_4]^{4-}$, which were investigated in previous TRXL studies[11,12]. To generate difference scattering curves, we assumed a simple structural change of 1% size increase of $[Ir_2(dimen)_4]^{2+}$ and $[Pt_2(P_2O_5H_2)_4]^{4-}$. To do so, we elongated the distances of all atomic pairs in the crystal structure by 1 % and calculated a difference scattering curve arising from the structural difference between the expanded structure and the crystal structure. Difference scattering curves were calculated considering all the constituent atoms or only heavy atoms (two Ir atoms for $[Ir_2(dimen)_4]^{2+}$ and two Pt atoms for $[Pt_2(P_2O_5H_2)_4]^{4-}$). As can be seen in Figs. S2b and S2c, the contributions of the ligands to the scattering intensity are no longer negligible, unlike the case of the gold trimer complex.

We also compared the contributions of the solute and the cage terms to the scattering intensity. The cage term was calculated from the pair distribution functions between solute and solvent molecules obtained from molecular dynamics simulations. As can be seen in Fig. S3, the total scattering intensity of the gold trimer complex is almost the same as the solute term and the contribution of the cage term is negligibly small, since the x-ray scattering factor of a gold atom is dominant compared with the scattering factors of hydrogen and oxygen atoms of the solvent molecule. Considering the negligible contributions of the ligands and the cage term to the scattering intensity, the gold trimer complex can be approximated as a triatomic molecule in terms of x-ray scattering signal.

8. Prospect with LCLS-II HE for solute molecules without heavy atoms

With the advance of XFEL technology, TRXL will be applicable to a wide variety of systems other than molecules containing heavy atoms. For example, the next-generation LCLS (LCLS-II HE) will be in operation in the near future and provide x-ray pulses of much higher photon flux than currently-running XFELs; specifically it will have 1000 times higher photon flux than PAL-XFEL. As a result, the signal-to-noise ratio of the data measured with LCLS-II HE would be improved by ~32 times (= square root of 1000) for a given measurement time, for example, compared with the data measured at PAL-XFEL presented in this work. As a result, LCLS-II HE would allow the detection of weak time-resolved scattering signal from molecules consisting of only light atoms such as carbon, nitrogen, and oxygen. To examine the feasibility of TRXL experiment on molecules consisting of only light atoms, we considered a model system of oxygen trimer, O_3, for direct comparison with the gold trimer investigated in this work. Because the amplitude of difference x-ray solution scattering is proportional to the square of the number of electrons (Au: 79 electrons, O: 8 electrons), O_3 is expected to give smaller TRXL signal by 100 times than the gold trimer. Such deficiency of the scattering intensity of light atoms can be compensated for by significant increase of photon flux at LCLS-II HE. For O_3 in solution, we simulated a TRXL experiment at LCLS-II HE by assuming 1000 times more photons per second than at PAL-XFEL and data accumulation for 48 hours.

In the simulation, we considered an asymmetric stretching mode of O_3 with ΔR_{AB} = 0.24 Å, ΔR_{BC} = 0.09 Å, ΔR_{AC} = 0 Å, the oscillation period of 1 ps, and the damping constant of 1 ps. The concentration of O_3 solution was set to be 3 mM in water solvent. Mock

difference scattering curves for O_3 were calculated for time delays from –300 fs to 2500 fs with a time step of 50 fs. A static scattering curve at each time delay was calculated using Debye equation and added to a static scattering curve of water solvent that was experimentally obtained in a separate experiment. Then, random statistical error for each q point was generated assuming a Gaussian distribution with a standard deviation value at LCLS-II HE, $\sigma_{LCLS-II\,HE}(q)$. $\sigma_{LCLS-II\,HE}(q)$ was calculated from the standard deviation value at PAL-XFEL, $\sigma_{PAL-XFEL}(q)$, obtained from the measurement of static scattering curve of water solvent, as follows,

$$\sigma_{LCLS-II\,HE}(q) = \sigma_{PAL-XFEL}(q)\sqrt{\frac{N_{LCLS-II\,HE}}{N_{PAL-XFEL}}} \tag{S10}$$

where $N_{LCLS-II\,HE}$ is the photon flux at LCLS-II HE (= 3×10^{16} photons/s) and $N_{PAL-XFEL}$ is the photon flux at PAL-XFEL (= 3×10^{13} photons/s).

Random errors were generated for scattering curves at all time delays. Scattering curves at a reference time delay (that is, –300 fs) were generated in the same manner and subtracted from scattering curves at time delays from –300 fs to 2500 fs, resulting in mock time-resolved difference scattering curves. These procedures were performed repeatedly to simulate the data accumulated for 48 hours.

In Fig. S4a, the mock time-resolved difference scattering curves at three representative time delays separated by a half period (500 fs) of the asymmetric stretching mode are shown (red curves). In addition, difference scattering curves generated without the random errors are shown together (black curves). We performed singular value decomposition analysis on the mock scattering curves. The first left and right singular vectors (lSVs and rSVs) for the mock scattering curves and the error-free mock scattering curves are shown by red and black curves, respectively, in Fig. S4b. From the comparison of the first singular vectors of the data sets with and without errors, we can expect that the simulated experimental conditions (data collection at LCLS-II HE for 48 hours) can yield a data set with a sufficient signal-to-noise ratio to recognize oscillatory features in q-axis and time-axis. Especially, temporal oscillation of the scattering data with an oscillation period of 1 ps is clearly resolved, demonstrating that molecular vibrations of molecules containing only light atoms can be visualized by the TRXL experiment performed with LCLS-II HE.

To check whether such TRXL experiment on O_3 in solution is feasible using currently available XFEL facilities, we performed another simulation of TRXL experiment at PAL-XFEL as an example. For this simulation, we used a standard deviation value at PAL-XFEL, $\sigma_{PAL-XFEL}(q)$, to generate random statistical error. Other parameters for the simulation were fixed to the same values used for the simulation for LCLS-II HE. In Fig. S4c, the mock time-resolved difference scattering curves (red curves) and difference scattering curves generated without the error (black curves) at time delays of 50 fs, 550 fs, and 1050 fs are shown. The first lSV and rSV for the mock scattering curves and the error-free mock scattering curves are shown by red and black curves, respectively, in Fig. S4d. As can be seen from the first singular vectors of the data set with error, it is difficult to obtain a sufficient signal-to-noise ratio enough to resolve the oscillation of O_3 by the TRXL experiment at PAL-XFEL., indicating that vibrations of molecules containing only light atoms is hard to be observed using currently available XFEL facilities.

9. Contribution of monomers, dimers and trimers to time-resolved difference scattering curves, $q\Delta S(q,t)$

The sample solution was prepared with the initial concentration of monomers being 300 mM. The prepared solution approaches the equilibrium with the dimers and trimers being formed with the aggregation of monomers, and the solution at equilibrium[17] contains 60 mM of monomers, 69 mM of dimers, and 34 mM of trimers[9]. Note that, with the concentrations and extinction coefficients of those species in this solution at equilibrium, $q\Delta S(q,t)$ is dominated by the contribution of trimers. Because monomers have a negligibly small extinction coefficient and do not involve any photo-induced structural change, the contribution of the monomers to $q\Delta S(q,t)$ can be completely ignored. Although the concentration of dimers (69 mM) is about twice larger than that of trimers (34 mM), the extinction coefficient of dimers (1.2×10^2 cm^{-1}M^{-1}) is about 27 times smaller than that of trimers (3.2×10^3 cm^{-1}M^{-1})[9]. In addition, $q\Delta S(q,t)$ arising from one trimer is about three times larger than that from one dimer because a trimer has three Au-Au pairs and a dimer has only one Au-Au pair. Considering those factors, the dimer contribution to $q\Delta S(q,t)$ is expected to be less than 3 % compared with the trimer contribution[9]. Consequently, $q\Delta S(q,t)$ is predominantly determined by the photoreaction of the trimers.

Table S1. Structural parameters of refined equilibrium structures of $[Au(CN)_2^-]_3$

Asymmetric S_0

Parameter	Fit value	Error
R_{AB} (Å)	3.13	0.004
R_{BC} (Å)	3.38	0.004
Au-Au-Au angle (°)	119	0.3
Debye-Waller factor for R_{AB} and R_{BC}, σ_1^2 (Å^2)	0.08	0.001
Debye-Waller factor for R_{AC}, σ_2^2 (Å^2)	0.23	0.007

Symmetric S_0

Parameter	Fit value	Error
R_{AB} (= R_{BC}) (Å)	3.26	0.002
Au-Au-Au angle (°)	119	0.3
Debye-Waller factor for R_{AB} and R_{BC}, σ_1^2 (Å^2)	0.09	0.001
Debye-Waller factor for R_{AC}, σ_2^2 (Å^2)	0.23	0.007

T_1'

Parameter	Value	Error
R_{AB} (Å)	2.82 (fix)	–
R_{BC} (Å)	2.82 (fix)	–
Au-Au-Au angle (°)	180 (fix)	–
Debye-Waller factor for R_{AB} and R_{BC}, σ_1^2 (Å^2)	0.08	0.002
Debye-Waller factor for R_{AC}, σ_2^2 (Å^2)	0.33	0.004

T_1

Parameter	Value	Error
R_{AB} (Å)	2.71 (fix)	–
R_{BC} (Å)	2.71 (fix)	–
Au-Au-Au angle (°)	180 (fix)	–

Black: azimuthally averaged difference scattering curve
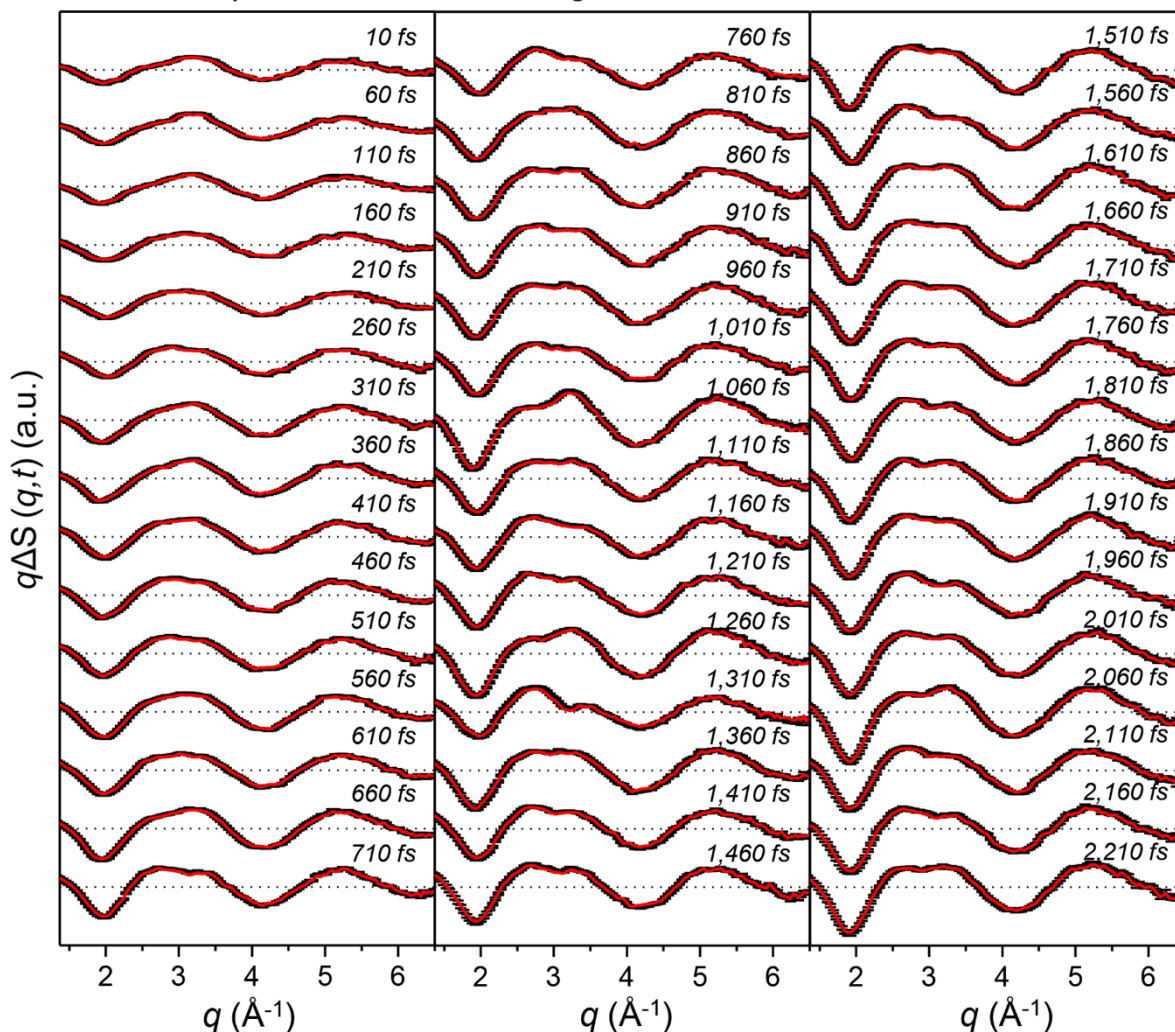Red: isotropic difference scattering curve

Figure S1. Time-resolved difference scattering curves, $q\Delta S(q,t)$, of $[Au(CN)_2^-]_3$ obtained by azimuthal average of two-dimensional scattering images (black). For comparison, isotropic difference scattering curves were generated from the scattering images (red). The two data sets are identical to each other within experimental errors, indicating that azimuthally averaged difference curves used in this work are practically identical to the isotropic difference scattering curves. For analysis, the azimuthally averaged difference curves were used since they have actually measured experimental errors and a better signal-to-noise ratio.
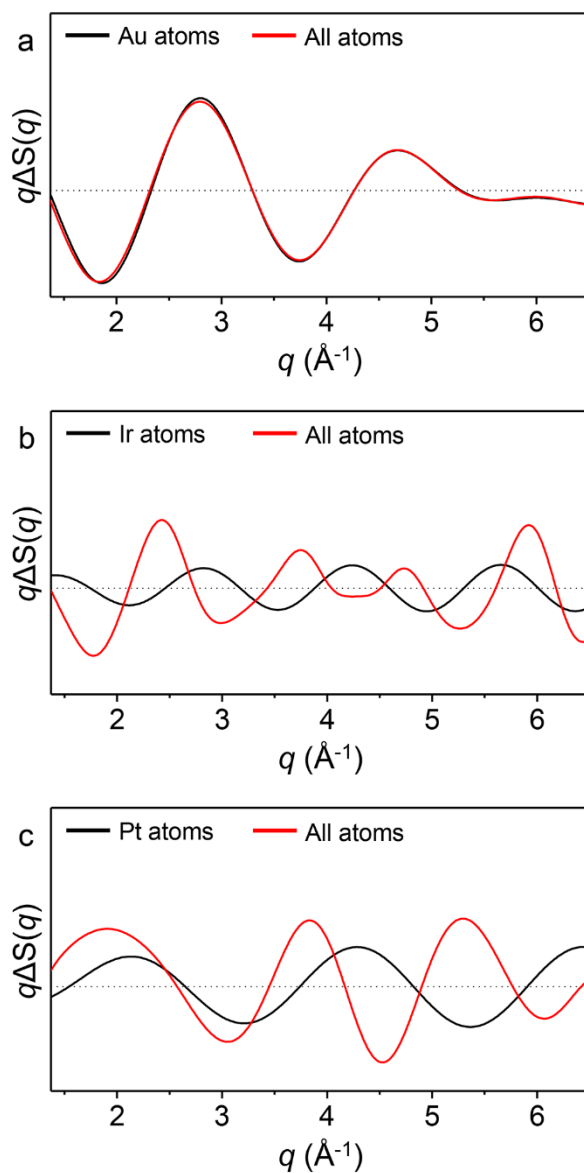
Figure S2. (a) The scattering pattern of the gold trimer complex considering all the constituent atoms (red) is almost the same as the scattering pattern of only three Au atoms (black) because the scattering intensities from C and N atoms are negligibly small, and thus the gold trimer complex can be approximated as a triatomic molecule in terms of x-ray scattering signal. In the cases of $[Ir_2(dimen)_4]^{2+}$ (b) and $[Pt_2(P_2O_5H_2)_4]^{4-}$ (c) for comparison, the contributions of the ligands are no longer negligible.
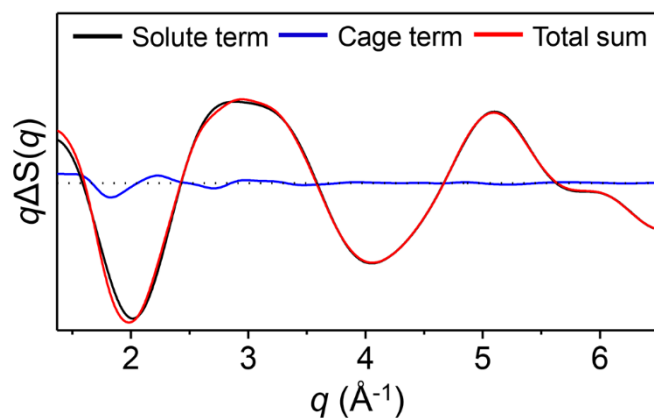
Figure S3. The total scattering pattern of the gold trimer complex is almost the same as the scattering pattern of the solute-only term because the contribution of the cage term is negligibly small. In the case of the gold trimer complex, the contribution of the cage term becomes negligible since the x-ray scattering factor of the gold atoms is dominant compared with the scattering factors of hydrogen and oxygen atoms of the solvent molecule.
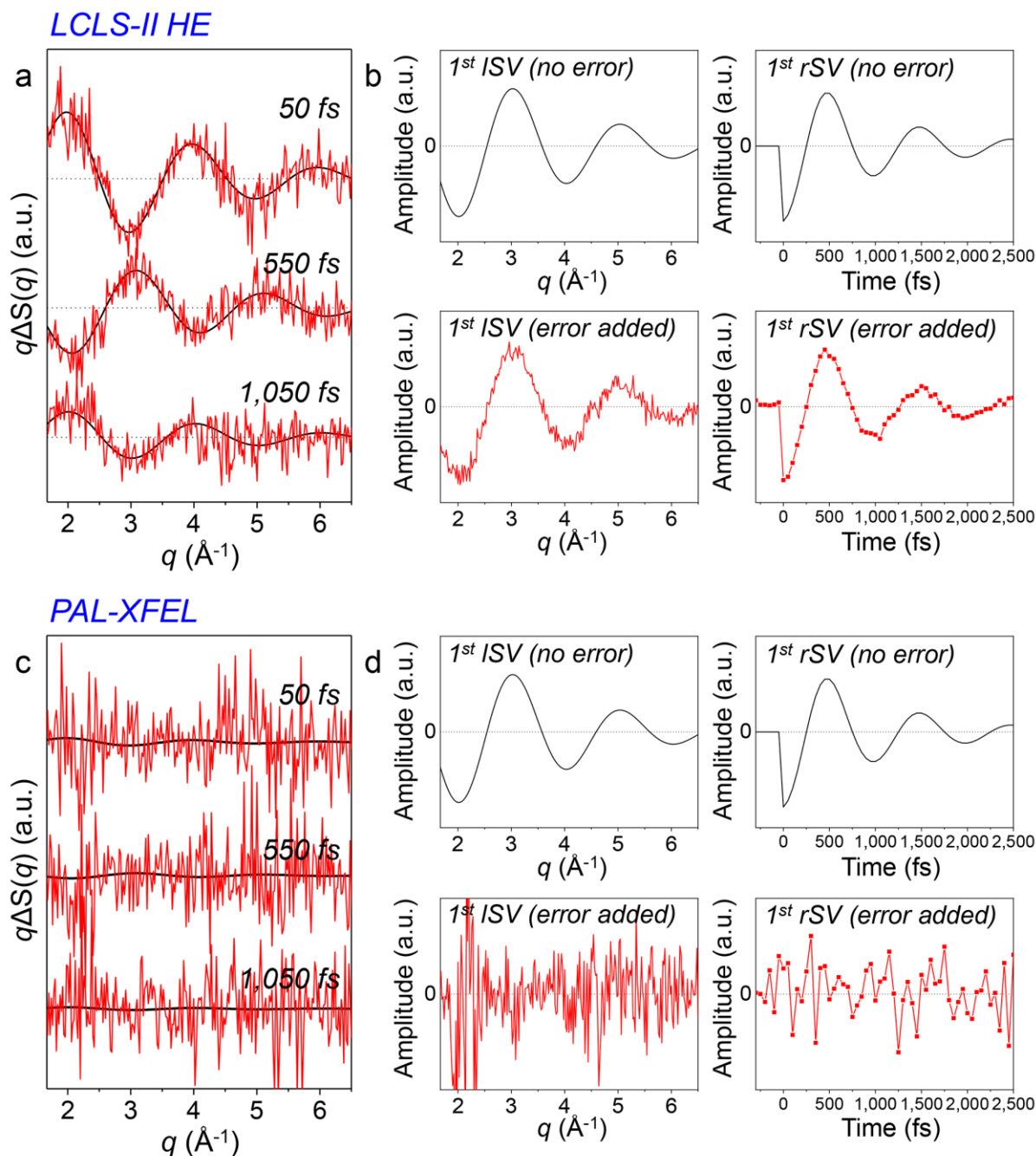
Figure S4. Simulation of TRXL experiment on O_3 in solution at LCLS-II HE. We assumed that O_3 molecules in solution vibrate following an asymmetric stretching mode and calculated mock time-resolved difference scattering curves at time delays from –300 fs to 2500 fs with a time step of 50 fs. See supplementary text for details of the simulation. (a) Mock time-resolved difference scattering curves at three representative time delays separated by a half period of the asymmetric stretching mode, without (black curves) and with (red curves) considering random statistical errors. The scattering curves with random statistical errors

were obtained by simulating TRXL data at LCLS-II HE with data accumulation for 48 hours. (b) Result of SVD analysis performed on the mock TRXL data without (upper panels) and with (lower panels) errors. To compare with TRXL experiment using currently available XFEL facilities, we performed another simulation of TRXL experiment on O_3 in solution at PAL-XFEL as an example, considering the photon flux at PAL-XFEL while other parameters were fixed to the same values used for the simulation for the case of LCLS-II HE. Mock time-resolved difference scattering curves and SVD results are shown in (c) and (d), respectively.
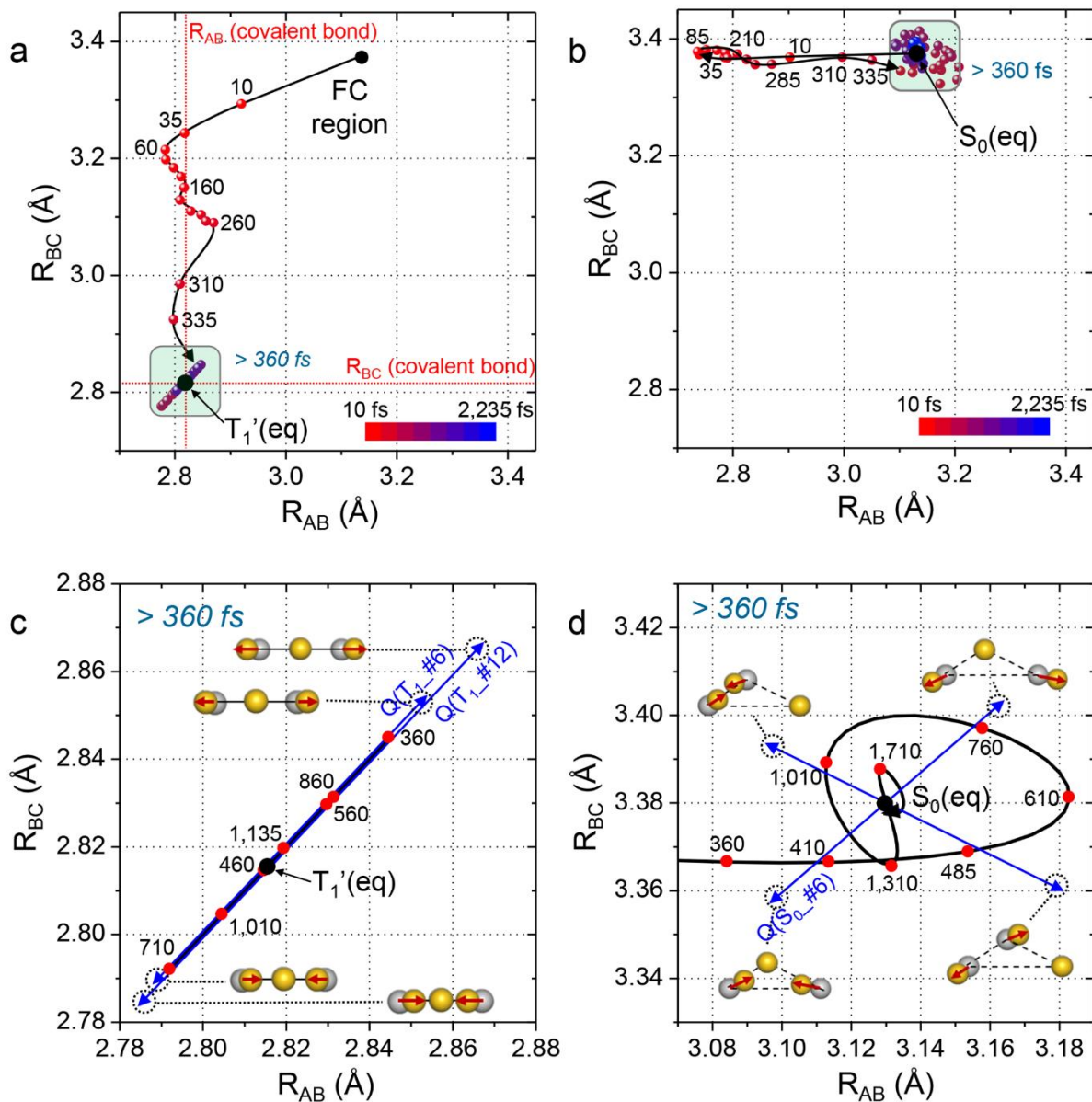
Figure S5. (a, b) The projection of wave packet motion shown in Fig. 3a and 3c onto the R_{AB}–R_{BC} plane. The trajectory of the wave packet over time is shown by a black curved arrow and, in (a), the equilibrium distances of R_{AB} and R_{BC} in T_1' are indicated by red vertical and horizontal dotted lines, respectively. The positions of the wave packet at measured time points are indicated by dots, whose colors represent time delays based on a color scheme shown at the bottom of each panel. For several representative time delays, the time delays in femtoseconds units are shown next to the corresponding wave packet position. The harmonic oscillations of the wave packets in T_1' and S_0 in the late time range (> 360 fs) are indicated by blue-shaded areas. (c, d) Late time-range (> 360 fs) trajectories of the excited-state wave packet in T_1' (c) and the ground-state wave packet in S_0 (d) represented in the R_{AB}–R_{BC} plane.

These plots correspond to a magnified view of the blue-shaded areas in (a) and (b), respectively, for clear presentation of the harmonic oscillations. The normal coordinates of the two symmetric stretching modes, $Q(T_1\_\#6)$ and $Q(T_1\_\#12)$, for T_1' (c) and the symmetric and asymmetric stretching modes, $Q(S_0\_\#6)$ and $Q(S_0\_\#5)$, for S_0 (d) are indicated by blue arrows. The displacements of three Au atoms by each normal mode are represented by yellow dots while the positions of Au atoms in the equilibrium structures are represented by grey dots. The displacement vectors of Au atoms for each mode are indicated by red arrows on the corresponding equilibrium structure. For each mode, the displacements of Au atoms are exaggerated for clarity.